

MIT Open Access Articles

Analysis of PV Drains for Mitigation of Seismically Induced Ground Deformations in Sand Slopes

The MIT Faculty has made this article openly available. **Please share** how this access benefits you. Your story matters.

Citation: Vytiniotis, Antonios, and Andrew J. Whittle. "Analysis of PV Drains for Mitigation of Seismically Induced Ground Deformations in Sand Slopes." *Journal of Geotechnical and Geoenvironmental Engineering* 143, 9 (September 2017): 04017049

As Published: [http://dx.doi.org/10.1061/\(ASCE\)GT.1943-5606.0001722](http://dx.doi.org/10.1061/(ASCE)GT.1943-5606.0001722)

Publisher: American Society of Civil Engineers (ASCE)

Persistent URL: <http://hdl.handle.net/1721.1/117512>

Version: Author's final manuscript: final author's manuscript post peer review, without publisher's formatting or copy editing

Terms of use: Creative Commons Attribution-Noncommercial-Share Alike



ANALYSIS OF PV DRAINS FOR MITIGATION OF SEISMICALLY-INDUCED GROUND DEFORMATIONS IN SAND SLOPES

by

Antonios Vytiniotis¹, M. ASCE, P.E. & Andrew J. Whittle², M. ASCE, P.E.

ABSTRACT: Prefabricated Vertical (PV) drain arrays have been proposed as a minimally-intrusive technique for mitigating seismically-induced ground deformations in sandy liquefiable slopes. This paper describes the representation of individual PV drains as line elements within the OpenSees finite element program. The elements can represent laminar or fully-turbulent discharge regimes, based on classic Darcy-Weisbach pipe flow, as well as fluid storage above the water table. Two-dimensional, plane strain simulations of coupled flow and deformation are performed using the proposed PV drain elements, with equivalent permeability properties for the surrounding soil mass, and the Dafalias-Manzari (DM2004) model to describe non-linear effective stress-strain behavior of the sand. The numerical predictions are evaluated through comparisons with pore pressures and deformations measured in a centrifuge model test. The results highlight the role of the PV drains and their discharge characteristics in controlling deformation mechanisms.

Keywords: Finite element analysis, earthquake engineering, centrifuge scale modeling, hazard mitigation, PV drains

¹ Exponent Failure Analysis Inc., 9 Strathmore Rd, Natick, MA, 01760, e-mail: avytiniotis@exponent.com

² Professor, Massachusetts Institute of Technology, 77 Massachusetts Avenue, Cambridge, MA, 02139

1 INTRODUCTION

2 There are a variety of soil improvement methods that can be used to reduce liquefaction
3 susceptibility of loose sands. Most of the standard methods rely on some form of mechanical
4 improvement of the soil mass through either in situ densification methods such as dynamic
5 compaction (Mitchell et al., 1995), vibroflotation, vibro-replacement and cementation methods
6 such as jet grouting, deep soil mixing, or compaction grouting (Adalier et al., 1998; Priebe, 1998;
7 Miller and Roycroft, 2004; Boulanger and Hayden, 1995), or stone/gravel columns (e.g., Seed and
8 Booker, 1977), which enhance drainage and also strengthen the soil mass. Some of these
9 techniques produce significant disturbance within the soil mass and hence, have limited
10 applicability in retrofit projects. In contrast, a number of ‘minimally intrusive’ liquefaction
11 mitigation techniques have also been proposed including PV drains, (Rathje et al., 2004; Rollins
12 et al., 2003) and permeation grouting using colloidal silica that forms a gel within the pore space
13 (Gallagher and Mitchell, 2002, Diaz-Rodriguez et al., 2008). While the effectiveness of these
14 techniques have been demonstrated through physical and full-scale model tests (e.g., Rollins et al.,
15 2003; Gallagher et al., 2007; Howell et al., 2012; Marinucci et al., 2008; Kamai et al., 2008), there
16 remains a lack of validated design methods for these methods of ground improvement.

17 This paper focuses on the effectiveness of PV drain systems for mitigating liquefaction and
18 cyclic mobility in sloping sand fills. The PV drains proposed for this application comprise high
19 flow capacity, perforated plastic pipes (with inside diameter, $D=75\text{mm} - 200\text{mm}$) that are encased
20 in geosynthetic filter fabric (Figure 1). The drains are typically installed in a grid pattern using a
21 mandrel that is vibrated into the ground and then withdrawn. The drain spacing, d_e , is currently
22 designed to limit the development of excess pore pressures ($r_{u,max} = |\Delta p / \sigma'_{v0}|_{max}$ where p is the pore
23 pressure, and σ'_{v0} the initial in situ vertical effective stress) within the soil. This is achieved by

balancing the undrained generation and dissipation of excess pore pressures during a design earthquake, characterized in this study by the bracketed duration of the event, t_d , the equivalent number of uniform shear stress cycles of loading, N_{eq} , and the number of uniform cycles of undrained shearing of a representative magnitude necessary to cause initial liquefaction, N_l .

Seed and Booker (1977) proposed analyses for the case of gravel drains assuming radial flow within a homogeneous soil mass and infinite vertical drain transmissivity ('perfect sink' representation). They developed design charts linking the maximum excess pore pressure ratio, $r_{u,max}$, to the spacing ratio, $r_s = D/d_e$, the time factor associated with the normalized duration, $T_{ad} = 4C_v t_d / (D)^2$, and seismic loading conditions ($r_n = N_{eq}/N_l$) of the design earthquake as shown in Figure 2.

Onoue (1988) subsequently modified the design charts to include well resistance as an important factor affecting the performance of gravel drains, a feature confirmed by Boulanger et al. (1998) who also found significant changes in drain permeability due to transport of fine particles. Pestana et al. (1998) developed a more general non-linear numerical analysis program (FEQDRAINTM) following the same principles. This program specifically accounts for the head loss of the fluid flowing across the walls and along a PV drain, together with a range of boundary conditions that control the storage of water within the drain (drain storage capacity) and discharge at the ground surface as illustrated in Figure 3.

None of the existing design methods consider how the PV drains affect deformations within the soil mass. This is clearly a major limitation in evaluating their effectiveness as a mitigation solution, especially in sloping ground. This paper investigates the performance of PV drain systems through 2-D finite element analyses of coupled flow and deformation using the OpenSees program (Mazzoni et al., 2005). The analyses simulate PV drains using a new class of 1-D line

elements that can represent laminar or turbulent pipe flow regimes, while radial seepage from the surrounding soil is approximated using equivalent hydraulic conductivity properties (after Hird et al., 1992). Non-linear effective stress-strain behavior of the sand is represented using the DM2004 model proposed by Dafalias and Manzari (2004). This paper evaluates predictive capabilities of the analyses using data from a centrifuge model test (SSK01; Kamai et al., 2008). The results show how the assumed PV flow regime affects the predicted drainage conditions within the soil mass, while comparisons with the measured data are used to understand how drainage limits lateral spreading.

PV-DRAIN ELEMENTS

Full-bore flow inside pipes (such as PV-drains) is commonly modeled through the Darcy-Weisbach equation that relates the frictional pressure loss, Δp , to the average fluid velocity, v . For a circular pipe:

$$\Delta p = \lambda \cdot \frac{L}{D} \cdot \frac{\rho v^2}{2} \quad (1)$$

where L and D are the length and inner diameter of the pipe respectively, ρ the mass density of water, and λ is a dimensionless friction factor controlled by the wall roughness and Reynolds number, Re (where $Re = \rho v D / \mu$, with μ being the dynamic viscosity of the draining fluid) after Moody (1944).

For laminar flow ($Re < 2300$), the friction coefficient is inversely proportional to Re ($\lambda = 64 / Re$) and using equation (1) the flow rate can be written in a rate form:

$$Q = C_l \frac{\Delta p}{L} \quad (2a)$$

$$\dot{Q} = \frac{A_f \cdot D^2}{32 \cdot \mu \cdot L} \dot{\Delta p} = \frac{C_l}{L} \dot{\Delta p} \quad (2b)$$

1

2 where A_f is the wetted area (i.e., $\pi D^2/4$ for full-bore flow) of the drain and the laminar drain
3 coefficient, $C_l = A_f D^2 / 32 \mu$.

4 Similarly, in the fully turbulent regime, the friction factor λ is constant and is controlled
5 by the wall roughness. The flow can be expressed as:

$$Q = C_t \sqrt{\frac{\Delta p}{L}} \quad (3a)$$

$$\dot{Q} = \sqrt{\frac{2 \cdot D \cdot A_f^2}{\lambda \cdot L \cdot \rho}} \cdot \frac{1}{2\sqrt{\Delta p}} \cdot \Delta \dot{p} = C_t \frac{1}{2\sqrt{\frac{\Delta p}{L}}} \frac{\Delta \dot{p}}{L} \quad (3b)$$

6 where the fully turbulent drain coefficient, $C_t = \sqrt{2 \cdot D \cdot A_f^2 / (\lambda \cdot \rho)}$.

7 The current analyses represent the PV drains as one-dimensional extended elements within
8 the OpenSees finite element program (Mazzoni et al., 2005). This approach implicitly decouples
9 the pipe flow from mechanical deformations of the drains (the current study does not consider
10 possible buckling of drains). Fluid pressures inside the pipe are assumed to match the external pore
11 pressures in the adjacent soil (i.e., there is no allowance for head loss through the pipe wall), and
12 the bending stiffness of the thin-walled drains is negligible. The resulting two-noded PV drain
13 elements have three degrees of freedom per node as shown in Figure 4, with generalized force and
14 displacement vectors given by:

$$\dot{\hat{q}} = [\dot{q}_1 \ \dot{q}_2 \ \dot{Q}_1 \ \dot{q}_3 \ \dot{q}_4 \ \dot{Q}_2]^T \quad (4a)$$

$$\dot{\hat{u}} = [\dot{u}_1 \ \dot{u}_2 \ \dot{p}_1 \ \dot{u}_3 \ \dot{u}_4 \ \dot{p}_2]^T \quad (4b)$$

1 where \dot{u}_i and \dot{q}_i are the rates of nodal displacement and force components respectively; \dot{p}_i and \dot{Q}_i
 2 are the rates of nodal pore pressures and axial flow respectively.

3 The generalized equilibrium of the finite element can be written:

$$\begin{bmatrix} \dot{q}_1 \\ \dot{q}_2 \\ \dot{Q}_1 \\ \dot{q}_3 \\ \dot{q}_4 \\ \dot{Q}_2 \end{bmatrix} = \begin{bmatrix} k_{11} & k_{12} & 0 & -k_{11} & -k_{12} & 0 \\ k_{12} & k_{22} & 0 & -k_{12} & -k_{22} & 0 \\ 0 & 0 & k_{33} & 0 & 0 & -k_{33} \\ -k_{11} & -k_{12} & 0 & k_{11} & k_{12} & 0 \\ -k_{12} & -k_{22} & 0 & k_{12} & k_{22} & 0 \\ 0 & 0 & -k_{33} & 0 & 0 & k_{33} \end{bmatrix} \cdot \begin{bmatrix} \dot{u}_1 \\ \dot{u}_2 \\ \dot{p}_1 \\ \dot{u}_3 \\ \dot{u}_4 \\ \dot{p}_2 \end{bmatrix} \quad (5)$$

4 where $k_{11} = \cos^2 \theta \cdot \frac{AE}{L}$; $k_{12} = \cos \theta \cdot \sin \theta \cdot \frac{AE}{L}$; $k_{22} = \sin^2 \theta \cdot \frac{AE}{L}$; and AE is the axial stiffness
 5 of the thin-walled PV drain, and θ its orientation in the global coordinate system.

6 The formulation is completed through the definition of k_{33} that defines the incrementally-
 7 linearized relationship between pore pressure and flow rate. In the laminar regime this is obtained
 8 directly from the drain coefficient:

$$k_{33} = -\frac{A_f \cdot D^2}{32 \cdot \mu \cdot L} = -C_l \cdot \frac{1}{L} \quad (6)$$

9 In the fully turbulent regime the pressure-flow rate relation is non-linear. The numerical
 10 implementation considers an increment in the nodal water pressures at time i , and the resulting
 11 flow rate in this time step, δQ_i :

$$\delta \Delta p^i = \delta p^i_2 - \delta p^i_1 \quad (7a)$$

$$\delta Q^i = Q(\Delta p^i + \delta \Delta p^i) - Q(\Delta p^i) \quad (7b)$$

12 From which the ‘consistent’ stiffness coefficient can be derived:

$$k_{33}^i = \frac{\delta Q^i}{\delta \Delta p^i} \quad (8a)$$

This approach can generate numerical problems when the pore pressure difference or incremental pressure difference are very small (i.e., $\Delta p^i \approx 0$; $\delta \Delta p^i \approx 0$, thus the denominator is very close to zero). These cases are avoided by specifying a threshold pressure difference, d_c , with the following approximations as illustrated in Figure 4 (shown for $\Delta p^i > 0$, without any loss of generality):

$$\delta \Delta p_i < d_c \cap \Delta p_i > d_c: k_{33}^i = \sqrt{\frac{2 \cdot D \cdot A_f^2}{\lambda \cdot L \cdot \rho}} \cdot \frac{1}{2\sqrt{\Delta p^i}} \quad (8b)$$

$$\delta \Delta p_i < d_c \cap \Delta p_i < d_c: k_{33}^i = \frac{C_t}{\sqrt{d_c} \cdot L} \quad (8c)$$

We implemented the two element classes (i.e., laminar and fully turbulent regimes) within the OpenSees code. In practice, the groundwater table often lies well below the ground surface and PV drains are installed through overlying, partially saturated soil units. A variety of boundary conditions can be expected depending on the permeability of these surficial layers. This paper also considers the case where the surficial soils have low permeability and water fills the PV drain before discharge occurs at the ground surface. The storage capacity of each PV drain corresponds to the volume of fluid stored above the water table prior to discharge. As the proposed PV drain elements compute flow at every time-step, the total influx of water can be used to update the location of the water table inside the drain (H, Figure 3) and hence, the pore pressure at Point A.

Representation of Drains in 2-D analyses

Hird et al. (1992) have investigated the use of two-dimensional, plane strain finite element (FE) analyses for simulating quasi-static consolidation with arrays of PV drains. They show that a plane strain unit cell can achieve the same average degree of consolidation as an axisymmetric unit cell through the selection of an equivalent drain spacing, or through equivalent soil permeability

and equivalent drain transmissivity. When the drain spacing is the same in the axi-symmetric and plane strain configurations then the three dimensional flow can be matched in the plane strain model using an equivalent permeability of the soil, k_{pl} , as follows:

$$k_{pl} = \frac{2k_{ax}}{3[\ln(1/r_s) - 3/4]} \quad (9)$$

where k_{ax} is the permeability for the physical situation and r_s is the drain spacing ratio.

An equivalent drain transmissivity also needs to be introduced to match the same average degree of consolidation. By solving analytically the plane strain and axisymmetric horizontal flow towards a drain in a unit cell, the equivalent plane strain laminar flow coefficient can be approximated as:

$$C_l^{pl} = \frac{2}{\pi R} C_l^{ax} \quad (10)$$

The Appendix shows that the turbulent flow coefficient can be approximated linearly to the laminar flow coefficient for a range of pressures gradients, thus the equivalent plane strain fully turbulent flow coefficient can be approximated as (for a plane strain grid of width w):

$$C_t^{pl} = \frac{2}{\pi R} C_t^{ax} \sqrt{w} \quad (11)$$

Vytiniotis (2009) has confirmed that this approach achieves very close matching of the average degree of consolidation, there are differences in the spatial distribution of excess pore pressures between the equivalent plane strain and radial drainage models. The current analyses tend to overestimate the excess pore pressures mid-way between drains. However, this discrepancy is readily justified by the large computational advantage associated with the 2D model.

The Appendix shows that in order to appropriately scale efflux rates through a PV drain between prototype and model scales it is important to consider the specific flow regimes (i.e., laminar vs. turbulent). If appropriate efflux scaling is used, the Reynolds number (Re) differs between the scale-model and prototype (assuming the same fluid is used in both cases). Thus, it is possible that turbulent flow in a prototype PV drain can correspond to laminar flow at model-scale. Given this discrepancy, the Appendix proposes a methodology to design model-scale PV drains that match the flow in prototype scale drains more accurately and to evaluate, a priori, the effect of turbulence on drain outflow rates.

EVALUATION OF NUMERICAL FRAMEWORK USING CENTRIFUGE MODEL

The numerical procedures dealing with the simulation of the PV-drains have been validated through finite element modeling of a reference centrifuge model test, SSK01 (Kamai et al., 2008) conducted in the 9-meter radius centrifuge at University of California (UC) Davis operating at a gravitational acceleration of 15 g ($N=15$). The test compares the response of two similar facing slopes with a central channel (Figure 5). Beneath the left side slope, is a layer of loose sand containing an array of perforated nylon PV-drains, while the right side slope is underlain by untreated, loose sand. The model PV drains were placed prior to pluviation of the surrounding sand and hence, there are no local densification effects associated with drain installation. The two sides both comprise three distinct soil layers: 1) a base layer of dense fine Nevada Sand, with relative density, $D_r=84\%$; 2) a “liquefiable” layer of loose Nevada Sand, $D_r=40\%$; and 3) a cap layer of compacted (low permeability) Yolo Loam.

Nevada sand is a fine sand ($D_{50}=1$ mm, $\gamma_{d,max}=17.33$ kN/m³, $\gamma_{d,min}=13.87$ kN/m³) and was placed by dry pluviation. The Yolo Loam is a clayey silt (with plasticity index, $I_p = 13\%$) and was placed in multiple lifts compacted by gentle tamping. It impedes vertical dissipation of pore water from the liquefiable layer.

The model was subjected to a sequence of five harmonic shaking events with period, $T=0.5$ s, and maximum accelerations $a_{max}=0.01, 0.03, 0.07, 0.11, 0.3$ g. All events were applied transverse to the central channel in the longitudinal direction. Figure 5a illustrates part of the model instrumentation that included i) arrays of accelerometers and pore-pressure transducers within the loose sand; and ii) displacement transducers to measure vertical and horizontal displacements at the surface of the Yolo loam. The current analysis considers only the third loading sequence (named SSK01_10) with maximum applied horizontal acceleration, $a_{max}=0.07$ g. This is the first event involving significant generation of excess pore pressures and ground deformations and hence, the most credible for model validation.

Finite Element Model

The finite element analysis is performed at prototype scale. Figure 5b illustrates the main features of the OpenSees finite element model used to simulate the centrifuge model test:

1. Coupled flow and deformation in the high permeability sand layers are represented by 4-noded QuadUP elements with bilinear interpolation of displacements and pore pressures. Although these elements have limitations when modeling incompressible behavior (i.e., they do not satisfy Babuska-Brezzi conditions for undrained shearing of saturated soil; cf., Oden and Carey, 1984), the Authors have found no problems in the current analyses where partial

1 drainage prevails throughout the sand layer. The element size was selected to be approximately
2 0.2m in order to prevent aliasing of seismic waves based on the known frequency of the applied
3 excitation and computed stiffness properties of the soils. The high spatial resolution also
4 enables good interpolation of deformations and pore pressures between the lines of PV drains.
5 The effective stress-strain-strength properties of the Nevada sand layers are modeled using the
6 DM2004 model (with parameters described in the next section).

7 2. Time stepping is accomplished using the Krylov subspace acceleration Newton algorithm
8 (Scott & Fenves, 2010). The time step-size was varied dynamically in order to achieve
9 efficient convergence to the specified energy error norm. Numerical accuracy was established
10 by comparing the computed results over a range of tolerances.

11 3. The capping layer of Yolo loam is represented by 4-noded Quad elements (bi-linear
12 displacement interpolation using total stresses), and its undrained shear properties are
13 represented by an elastic, perfectly-plastic model (Mazzoni et al., 2005).

14 4. Displacements of contact nodes between QuadUP and Quad domains are tied together (i.e.,
15 there is no slippage between the sand and the loam layers).

16 5. The centrifuge model is built within a laminar box (flexible shear beam container). Periodic
17 boundary conditions are applied at the sides of the model (including the mass of the steel
18 plates). The sand layers are continuous across the model and hence, remain in contact with the
19 box walls throughout shaking. In contrast, the Yolo loam forms a partial cap and is absent in
20 the central channel.

21 6. The PV drain array is represented in the 2D numerical model by a series of 7 uniformly-spaced,
22 lines of laminar or turbulent flow drain elements with properties listed in Table 1. The water

table is located at the top of the sand layer in the centrifuge model, while the PV drains discharge at the ground surface (i.e., above the Yolo loam). Hence, there is a significant storage effect (i.e., water will move upwards in the PV-drains before discharging at the ground surface and effectively reducing excess pore pressures in the sand layers) that is also represented by the drain elements. The finite element approximation of planar flow is represented using an equivalent hydraulic conductivity. There is free flow occurring towards the central channel and closed flow boundaries along the sides and the base of the model. The sand is assumed to have in prototype scale a hydraulic conductivity of $k^p = 3 \times 10^{-4}$ m/s in the untreated region, and $k^p = 1 \times 10^{-4}$ m/s in the improved region to match the properties for radial flow into the drain. The input parameters needed for the PV drains are the transmissivity for laminar flow, the transmissivity for turbulent flow, the axial stiffness, and the storage capacity. The nylon drains have an inner diameter, $D^p = 105$ mm, and wall thickness, $w^p = 30$ mm (prototype scale). Table 1 summarizes the input parameters for the PV-drains at prototype scale, corresponding to a centrifuge model scaling factor, $N=15$.

7. Seismic loading is represented by applying a uniform horizontal excitation (acceleration) across the base of the model.

Soil Parameters

Although there are some uncertainties in the as-built density of the centrifuge model, the current analyses assume that the dense and loose Nevada sand are prepared uniformly with relative densities, $D_r = 80\%$ and 40% respectively. The DM2004 critical state elasto-plastic constitutive soil model is used to simulate the effective stress-strain properties of the sand during cyclic loading events. This model predicts reasonably well both the monotonic and the cyclic behavior of sand measured in laboratory element tests and is also able to capture the effects of void ratio and

1 confining stress with a single set of model input parameters. It simulates shear-induced volumetric
2 plasticity during loading and subsequent unloading paths. Input parameters for the DM2004
3 effective stress model have been calibrated for fine Nevada sand by Vytiniotis (2012) (Table 2)
4 and are used in the current numerical simulations. Figure 6 shows a typical comparison between
5 computed and measured behavior of medium-loose Nevada sand ($D_r = 50\%$; Kammerer et al.,
6 2000) for two-way cyclic undrained direct simple shear test, at an initial confining stress, $\sigma'_{vc}=35$
7 kPa. These results show reasonable agreement between the computed and measured effective
8 stress paths (i.e., accumulation of shear-induced pore pressures; Fig. 6a). The model also
9 accumulates shear strain with load cycles (Fig. 6b) but reaches a shakedown condition after 4 load
10 cycles (while the measured data shows further strain accumulation with little change in excess pore
11 pressure) number of cycles. For cases with an initial static shear stress, the DM2004 model can
12 also predict continuous accumulation of plastic strains, but the accuracy is varies with the obliquity
13 of the initial stress state (Vytiniotis, 2012).

14 The DM2004 model was implemented in the OpenSees software framework by the authors using
15 an explicit integration scheme with automatic sub-incrementation. To further improve the
16 integration of the model, a correction algorithm that returns the model state to the critical state or
17 the bounding surface line (whichever one is controlling based on the state of the sample) was
18 implemented as suggested by Potts and Gens (1985). Finally, a return-to-apex correction was
19 implemented. Vytiniotis (2012) presents full details of the model implementation.

20 Undrained shear properties of the Yolo loam are represented by an elasto-plastic model, with
21 shear stiffness dependent on the effective confining stress, and shear strength described by a von

Mises yield criterion with associated flow (using the PI-MYS nested yield model available in OpenSees, Mazzoni et al., 2005). Table 3 lists the input parameters for this model.

Interpretation and Evaluation of Computed Results

Laminar vs. Turbulent Drains

Figure 7 compares the computed pore pressures for the SSK01_10 event (i.e., $a_{\max}=0.07$ g) using laminar and turbulent drain elements at three elevations within the loose sand. As expected, there is greater accumulation of excess pore pressures in the lower sand on the untreated side of the model (F vs C). Differences in modeling the flow regimes have little effect on the untreated side of the model (points D, E, F). However, within the treated zone, pore pressures accumulate more rapidly for the analyses with fully turbulent PV drain elements showing that laminar flow assumption can lead to non-conservative results (i.e., greater computed pore pressure dissipation). At point C the analyses predict significantly higher excess pore pressures for turbulent drains as turbulence diminishes the discharge capacity of the PV-drains.

Drain Outflow

Figure 8 shows typical outflow results computed for one row of drains (#2, see Figure 5) during the cyclic loading event ($t \leq t_d = 10$ secs) and subsequent dissipation (3 secs). As discussed in the Appendix, when a scale model is designed so that the same excess pore pressures generation and dissipation occurs at model and prototype scales, the Reynolds numbers do not scale accordingly. Figure 8a shows that the calculated efflux of a single row of drains is above the laminar limit for a prototype scale model but remains just marginally above laminar if model-scale flow is considered. Thus in this simulation a fully-turbulent assumption would reduce the effective

permeability of the drains. For this reason, subsequent comparisons of simulations and experimental data are based on the laminar drain analysis.

This result also highlights the need to consider carefully the design of model-scale PV drains that appropriately simulate prototype-scale flow (using the procedure described in the Appendix). Figure 8b shows that, despite the cyclic nature of the loading the discharged volume increases steadily during the shaking event due to the continuous accumulation of excess pore pressures within the loose sand.

Soil Behavior

Figure 9 examines the effective stress paths (σ'_v, τ_w) and stress-strain (τ_w, γ) behavior at three points in the middle of the loose sand layer. Point A is midway between two PV-drains, B is adjacent to a PV drain, and C is located on the untreated side of the model (at the same elevations). Points A and C show similar behavior; the vertical effective stress decreases in each load cycle, and is constrained by the frictional strength of the sand ($\phi = 31^\circ$). Shear strains accumulate in each load cycle with diminishing levels of shear resistance. Point C reaches a state of “liquefaction” where $\sigma'_v \rightarrow 0$ and shows a notable amplification in cyclic shear strain with load cycles. There is a much smaller build-up of excess pore pressure, $\Delta u = -\Delta \sigma'_v$, at point B indicating that flow towards the PV-drains acts to stabilize the response of the loose sand and produces smaller accumulation of shear strains.

Comparisons with Measurements: Predicted Excess Pore Pressures

Figure 10 compares the predicted and measured pore pressures at six points within the loose sand. It is readily apparent from the measured data that PV drains are effective in reducing

1 excess pore pressures generated within the sand (compare time series for A vs. D at the top, B vs.
2 E in the middle or C vs. F towards the base of the sand).

3 The numerical analyses provide good predictions of the measured excess pore pressures in
4 the middle part of the untreated sand, E, but they underestimate the pore pressures occurring at the
5 top of the untreated sand, point D. This result occurs, in large part, because the ground water level
6 does not remain constant during the experiment due to sliding of the Yolo loam cap towards the
7 central channel (Kamai et al., 2008). It is also possible that the pore pressure transducer sank as
8 the untreated sand underwent liquefaction during the test.

9 The numerical analyses also predict slower dissipation of excess pore pressures after
10 cessation of shaking at point E, a feature that is related to the selected consolidation coefficient
11 (i.e., post shaking stiffness of the sand and its hydraulic conductivity) in the sand. There is
12 uncertainty in the actual value of the hydraulic conductivity of the placed sand layers and in its
13 variation during and after base shaking. At the bottom of the model (point F) the analysis
14 overpredicts excess pore pressures because closed flow boundaries misrepresent partial drainage
15 occurring at the sand/laminar box interface.

16 On the treated side of the model, direct comparison of the computed and measured pore
17 pressures (points A, B and C) should be interpreted with caution, since the plane strain analyses
18 match the average degree of consolidation in the sand surrounding the drains, not the spatial
19 variation of excess pore pressures (Vytiniotis, 2012). The equivalent plane strain analyses
20 generally predict higher excess pore pressures than those expected for a model with 3D flow at the
21 midpoint between the PV- drains as shown via a comparison between axisymmetric and plane
22 strain equivalent analyses in Vytiniotis (2009). This trend appears to be consistent with results at

points B and C. However, the numerical model predicts smaller excess pore pressures than the measured data at point A.

Displacements

Special care is needed when trying to interpret displacement measurements from centrifuge model tests because of non-uniformities in the gravitational field that affect the measured deformation mechanisms (Vytiniotis and Whittle, 2009). Figure 11 summarizes the computed and measured horizontal deformations for a series of 6 points along the surface of the Yolo loam cap. On the untreated side, the numerical analysis underestimates the lateral movements at points E and F (due to tension cracks that were observed in the Yolo loam), but is in very reasonable agreement with the experimental results at point D. On the treated side, the analysis results are in good agreement with the smaller movements measured above the PV drains.

Figure 12 compares the simulated lateral deformations along two vertical sections (on the treated and the untreated sides) at various times during shaking. For the untreated side, the results show that lateral spreading within the loose Nevada sand is partially constrained by the overlying Yolo loam cap. There is much smaller lateral spreading on the treated side of the model, confirming the efficacy of the PV drains in mitigating effects of liquefaction. Since the drain elements have no bending stiffness they have no effect on predicted lateral displacements.

Figure 13 compares the time-histories of the computed and measured vertical deformations at 6 points along the surface of the Yolo Loam. The finite element analyses correctly predict much smaller surface settlements on the treated side (points A, B and C). The comparisons on the untreated side vary from over-prediction at point F and E to relatively good agreement in point D.

Figure 14 shows that the numerical predictions of deformations are associated with a large rotational mechanism on the untreated side of the model.

CONCLUSIONS

One-dimensional drain elements have been developed to represent laminar or fully turbulent discharge through PV drains based on the Darcy-Weisbach pipe flow equation. The drain elements are implemented in the OpenSees finite element framework. Scaling laws describing modeling of PV drains in model-scale centrifuge experiments are presented. It is shown that the Reynolds number in prototype-scale inside the PV drains can be different than the number in model-scale, thus it is possible that the model-scale flow remains laminar whereas prototype flow is turbulent. The Appendix gives guidelines for experimentalists to select an appropriate model-scale drain dimensions that fits best the discharge of prototype drains.

The PV drain elements have been evaluated through comparisons with the measurements from a centrifuge model consisting of a loose sand slope improved with a PV drain system under a cyclic base excitation (event SSK01_10; Kamai et al., 2008). The numerical analyses incorporate the DM2004 (Dafalias and Manzari, 2004) model to represent the cyclic effective stress-strain properties of the loose Nevada sand. Overall, the numerical model provides reasonable qualitative agreement with observed pore pressures in the centrifuge model. However, the computed results are affected by uncertainties in the density and hydraulic conductivity of the loose sand layers and by partial flow at the base boundaries through the laminar box-sand interface. Simulation results further verify that flow towards the PV drains acts to stabilize the response of the loose sand and leads to smaller accumulation of shear strains in a slope improved with PV drains. Numerical

analysis indicates that, within the treated zone, pore pressures accumulate more rapidly for the analyses with fully turbulent PV drain elements showing that laminar flow assumption can lead to unconservative results.

ACKNOWLEDGEMENTS

The authors are grateful for support from NSF grant No. CMS-0530478, under the NEESR Grand Challenge project, “Seismic Risk Management for Port Systems”. The computations were performed on a cluster computer through the Center for Environmental Sensing and Modeling (CENSAM), part of the SMART program in Singapore. The first author also received support from the Alexander S. Onassis Public Benefit Foundation.

REFERENCES

- Adalier, K., Elgamal, A. K., & Martin, G. R. (1998). "Foundation liquefaction countermeasures for earth embankments." *Journal of Geotechnical and Geoenvironmental Engineering*, 10.1061/(ASCE)1090-0241(1998)124:6(500).
- Boulanger, R. W., Idriss, I. M., Stewart, D. P., Hashash, Y., & Schmidt, B. (1998). "Drainage capacity of stone columns or gravel drains for mitigating liquefaction." *Geotechnical Earthquake Engineering and Soil Dynamics III. 1*, Eds. P. Dakoulas, M. Yegian, and R. D. Holtz, 678-690.
- Boulanger, R. W., & Hayden, R. (1995). "Aspects of compaction grouting of liquefiable soil." *Journal of Geotechnical Engineering*, 10.1061/(ASCE)0733-9410(1995)121:12(844).
- Chiou, B., Darragh, R., Gregor, N., & Silva, W. (2008). "NGA project strong-motion database." *Earthquake Spectra*, 24(1), 23-44.
- Dafalias, Y., & Manzari, M. (2004). "Simple plasticity sand model accounting for fabric change effects". *Journal of Engineering Mechanics*, 10.1061/(ASCE)0733-9399(2004)130:6(622).
- Díaz-Rodríguez, J., Antonio-Izarraras, W., Bandini, P., & López-Molina, J. (2008). "Cyclic strength of natural liquefiable sand stabilized with colloidal silica grout." *Canadian Geotechnical Journal*, 45, 1345-1355.
- Gallagher, P., & Mitchell, J. (2002). "Influence of colloidal silica grout on liquefaction potential and cyclic undrained behavior of loose sand." *Soil Dynamics and Earthquake Engineering*, 22(9-12), 1017-1026.
- Gallagher, P., Conlee, C., & Rollins, K. (2007). "Full-scale field testing of colloidal silica grouting for mitigation of liquefaction risk." *Journal of Geotechnical and Geoenvironmental Engineering*, 10.1061/(ASCE)1090-0241(2007)133:2(186).
- Hird, C. C., Pyrah, I. C., & Russell, D. (1992). "Finite element modelling of vertical drains beneath embankments on soft ground." *Géotechnique*, 42(3), 499-511.
- Hosono, Y., & Yoshimine, M. (2004). "Cyclic behavior of soils and liquefaction phenomena." *Processing of the International Conference on Cyclic Behavior of Soils and Liquefaction Phenomena*, 129-136. Bochum, Germany.
- Howell, R., Rathje, E., Kamai, R., & Boulanger, R. W. (2012). "Centrifuge modeling of prefabricated vertical drains for liquefaction remediation." *Journal of Geotechnical and Geoenvironmental Engineering*, 10.1061/(ASCE)GT.1943-5606.0000604.

- 1 Kamai, R., Kano, S., Conlee, C., Marinucci, A., Boulanger, R. W., Rathje, E., Rix, G., Howell, R.
2 (2008). "Evaluation of the effectiveness of prefabricated vertical drains for liquefaction
3 remediation: Centrifuge data report for SSK01." Center for Geotechnical Modeling,
4 University of California at Davis.
- 5 Kamai, R., and Boulanger, R. W. (2013). "Simulations of a centrifuge test with lateral
6 spreading and void redistribution effects." *Journal of Geotechnical and*
7 *Geoenvironmental Engineering*, 10.1061/(ASCE)GT.1943-5606.0000845.
- 8 Kammerer, A. M., Pestana, J. M., Riemer, M., & Seed, R. (2002). "Cyclic simple shear testing
9 of Nevada sand for PEER center project 2051999." Research report No. UCB/GT/00-02,
10 University of California, Berkeley.
- 11 Marinucci, A., Rathje, E., Kano, S., Kamai, R., Conlee, C., Howell, R., Boulanger, R., and
12 Gallagher, P (2008). "Centrifuge testing of prefabricated vertical drains for liquefaction
13 remediation *Geotechnical Earthquake Engineering and Soil Dynamics IV, ASCE GSP 181,*
14 *1-10.*
- 15 Mazzoni, S., McKenna, F., & Fenves, G. (2005). "*Opensees Command Language Manual.*"
- 16 Miller, E. A., & Roycroft, G. A. (2004). "Compaction grouting test program for liquefaction
17 control." *Journal of Geotechnical and Geoenvironmental Engineering*,
18 10.1061/(ASCE)1090-0241(2004)130:4(355).
- 19 Mitchell, J. B. (1995). "Performance of improved ground during earthquakes." In R. Hryciw (Ed.),
20 *Soil Improvement for Earthquake Hazard Mitigation*, 1-36. San Diego, CA, ASCE
21 Convention.
- 22 Moody, L. F. (1944). "Friction factors for pipe flow." *Transactions of the ASME*, 66, 671-684.
- 23 Oden, J. T., & Carey, G. F. (1984). "*Finite Elements: Mathematical Aspects, Vol IV.*" Prentice-
24 Hall, Englewood Cliffs, NJ.
- 25 Onoue, A. (1988). "Diagrams considering well resistance for designing spacing ratio of gravel
26 drains." *Soils and Foundations*, 28(3), 160-168.
- 27 Pestana, J., Hunt, C., Goughnour, R., & Kammerer, A. (1998). "Effect of storage capacity on
28 vertical drain performance in liquefiable sand deposits." Proceedings of Second
29 International Conference on Ground Improvement Techniques, Singapore, 373-380.
- 30 Potts, D. M., & Gens, A. (1985). "A critical assessment of methods of correcting for drift from the
31 yield surface in elastoplastic finite element analysis." *International Journal for Numerical*
32 *and Analytical Methods in Geomechanics* , 9 (2), 149-59.

- 1 Priebe, H. J. (1998). "Vibro replacement to prevent earthquake induced liquefaction." *Ground*
2 *Engineering*, London.
- 3 Rathje, E. M., Chang, W. J., Cox, B. R., & Stokoe II, K. H. (2004). "Effect of prefabricated vertical
4 drains on pore pressure generation in liquefiable sand." *The 3rd International Conference*
5 *on Earthquake Geotechnical Engineering (3rd ICEGE)*. University of California,
6 Berkeley, CA.
- 7 Rollins, K., Anderson, J., McCain, A., & Goughnour, R. (2003). "Vertical composite drains for
8 mitigating liquefaction hazard." *13th International Offshore and Polar Engineering*
9 *Conference*, (pp. 498-505). Honolulu, Hawaii.
- 10 Scott, M.H. & Fenves, G.L. (2010) "Krylov subspace accelerated Newton algorithm:Application
11 to dynamic progressive collapse simulation of frames," *ASCE Journal of Structural*
12 *Engineering*, 136(5), 473-480.
- 13 Seed, H., & Booker, J. (1977). "Stabilization of Potentially Liquefiable Sand Deposits using
14 Gravel Drains." *Journal of the Geotechnical Engineering Division*, 103(GT7), 757-768.
- 15 Vytiniotis, A. (2009). "Numerical simulation of the response of sandy soils treated with pre-
16 fabricated vertical drains." SM Thesis, MIT Civil and Environmental Engineering
17 Department, Cambridge, MA.
- 18 Vytiniotis, A. (2012). "Contributions to the analysis and mitigation of liquefaction in loose sand
19 slopes." PhD Thesis, MIT Civil and Environmental Engineering Department, Cambridge,
20 MA.
- 21 Vytiniotis, A., & Whittle, A. J. (2009). "Effect of non-uniform gravitational field on seismically-
22 induced ground movements in centrifuge models." *2009 NSF Engineering Research and*
23 *Innovation Conference*. Honolulu, HI.
- 24 Whitman, R. V. (1985). "On liquefaction." *Proceedings of the 11th International Conference on*
25 *Soil Mechanics and Foundation Engineering*. San Francisco, CA.
- 26
- 27

1 APPENDIX: SCALING LAWS FOR PV-DRAINS

2 The efflux from a drain at prototype scale, Q^P , can be related to that at model scale, Q^M , as
 3 follows:

$$Q^P = \frac{\Delta V^P}{T^P} = \frac{\Delta V^M \cdot N^3}{T^M \cdot N} = \frac{\Delta V^M}{T^M} \cdot N^2 = Q^M \cdot N^2 \quad (12)$$

4 where T, N are the time and gravity scale in the model (superscript M stands for model-scale and
 5 superscript P for prototype-scale).

6 Similarly, the laminar and turbulent drain coefficients at prototype scale can be related to the model
 7 scale coefficients:

$$C_l^P \cdot \frac{\Delta P}{L^P} = C_l^P \cdot \frac{\Delta P}{N \cdot L^M} = C_l^M \cdot \frac{\Delta P}{L^M} N^2 \quad (13a)$$

$$C_l^P = C_l^M \cdot N^3 \quad (13b)$$

$$C_t^P \cdot \sqrt{\frac{\Delta P}{L^P}} = C_t^P \cdot \sqrt{\frac{\Delta P}{N \cdot L^M}} = C_t^M \cdot \sqrt{\frac{\Delta P}{L^M}} N^2 \quad (14a)$$

$$C_t^P = C_t^M \cdot N^{2.5} \quad (14b)$$

8 These relations show that the drain coefficient has to be N^3 times larger at prototype-scale when
 9 dealing with laminar flow drains and $N^{2.5}$ times larger for turbulent flow. The scaling relations
 10 indicate a potential problem that can arise due to differences in the Reynolds number at prototype
 11 and model-scales:

$$Re^P = \frac{V^P D^P}{\nu} = \frac{Q^P}{A^P} D^P = \frac{N^2 Q^M}{N^2 A^M} N D^M = \frac{Q^M D^M}{A^M \nu} N = Re^M N \quad (15)$$

12 i.e., since the Reynolds number in the prototype is N times larger than that at model-scale, a flow
 13 that is laminar in the model might be turbulent at prototype scale.

1 This is important as experiments that scale the geometric dimensions of the PV-drains by N, and
 2 use the same fluid (as the prototype), do not preserve Re at model-scale. Alternatively, if a different
 3 pore fluid is used in the centrifuge model (to scale the diffusion process, $v^P = v^M/N$), then the scaling
 4 ratio for Reynolds number is further increased:

$$\text{Re}^P = \text{Re}^M N^2 \quad (16)$$

5 Design of Model-Scale PV Drains

6 The selection of appropriate PV drain dimensions in scale-models can be achieved by estimating
 7 the error in prototype finite element simulations using laminar drains to model the fully turbulent
 8 flow in a real world scenario.

9 At prototype scale, the laminar flow parameter C_l should be selected to give the smallest error
 10 compared with the efflux from a drain with turbulent flow parameter C_t over a target range of
 11 pressure gradient in the PV drains, $i = \Delta P/L$. We define a minimum least squares residual error, F,
 12 between the laminar flow and the turbulent flow rates over a specific range of $i = (0, i_{\max})$:

$$f = (Q_t^P - Q_l^P)^2 = C_t^{P2} i^P + C_l^{P2} i^{P2} - 2C_t^P C_l^P i^{P\frac{3}{2}} \quad (17a)$$

$$F = \int_0^{i_{\max}} f \, di = \frac{C_t^{P2} i_{\max}^{P2}}{2} + \frac{C_l^{P2} i_{\max}^{P3}}{3} - \frac{4}{5} C_t^P C_l^P i_{\max}^{P\frac{5}{2}} \quad (17b)$$

13 By minimizing the value of F we find the prototype and model-scale laminar flow parameters C_l^P ,
 14 C_l^M that should be selected to give the smallest error compared with the efflux from a drain with
 15 prototype turbulent flow parameter C_t^P :

$$C_l^P = \frac{6C_t^P}{5\sqrt{i_{\max}^P}} \text{ and } C_l^M = \frac{6C_t^P}{5\sqrt{i_{\max}^P} \cdot N^3} \quad (18)$$

1 If we replace the expressions for C_l and C_t ($C_l = A_f D^2 / 32\mu$ and $C_t = \sqrt{2 \cdot D \cdot A_f^2 / \lambda \cdot \rho}$) we
 2 conclude:

$$C_l^M = \frac{A^M \cdot D^{M^2}}{32 \cdot \mu} = \frac{6}{5\sqrt{i_{max}^P} \cdot N^3} \sqrt{\frac{2 \cdot D^P \cdot A^{P^2}}{\lambda \cdot \rho}} \quad (19)$$

$$D^M = \left(\frac{77 \mu}{\sqrt{i_{max}^P} \cdot N^3} \sqrt{\frac{D^{P^5}}{2 \cdot \lambda \cdot \rho}} \right)^{\frac{1}{4}} \quad (20)$$

3 Eqn. 20 defines the scaling relation for the diameter of the PV drains at model and prototype
 4 scales (D^M , D^P , respectively) under the assumption that the flow is laminar at model scale and
 5 turbulent in the prototype. It can also be inverted to find the prototype diameter PV drain that a
 6 model-scale PV drain represents.

7 If the model and prototype situations use fluids of different viscosity, $\mu^P = \mu^M / N$:

$$D^M = \left(\frac{77 \mu^P}{\sqrt{i_{max}^P} \cdot N^2} \sqrt{\frac{D^{P^5}}{2 \cdot \lambda \cdot \rho}} \right)^{\frac{1}{4}} \quad (21)$$

8 Equations 20 and 21 provide a preliminary estimate of the effect of turbulence in simulating PV
 9 drains in FE models and in centrifuge tests.

10 The above equations provide preliminary estimation of the effect of turbulence in simulating PV
 11 drains in in centrifuge tests. For example, consider a prototype PV drain with properties
 12 ($\varepsilon/D=0.019$, $\mu=0.001\text{Pa}\cdot\text{s}$, $D=105\text{mm}$, $\lambda=0.05$). The maximum prototype pressure gradient for
 13 laminar flow ($\text{Re}<2300$) is $i_{max}=0.064\text{Pa/m}$. A researcher wants to model the PV-drains in a
 14 centrifuge box with $N=15$. He estimates that between prototype pressure gradients (0.064Pa/m ,

1 0.95Pa/m) the flow is laminar in the model scale but turbulent in the prototype scale. For a pressure
2 gradient of $i_{\max}=0.1\text{Pa/m}$ (consistent with pressure gradients calculated from the current analysis),
3 the corresponding model drain diameter would be $D^M=11\text{mm}$, i.e., 57% larger than that obtained
4 by scaling the drain diameter by N (7mm).

1 **Table 1 Drain properties at prototype scale for centrifuge test SSK01**

Category	Name	Value
	Inner Diameter, D (mm)	105
	Outer Diameter, D_{out} (mm)	135
	Cross Section, A (cm ²)	56.55
	Elastic Modulus, E (MPa)	3000
	Wetted Area, A_f (m ²)	0.0087
	Max. Stored Height (m)	1
	Laminar, C_l^{pl} (m ⁵ /kN) (eqn. 3)	0.1614
	Turbulent, C_t^{pl} (m ⁴ /kN ^{0.5} /s) (eqn. 3)	0.0247
	Hydraulic Conductivity, Untreated zone, k_{ax} (m/s)	3×10^{-4}
	Hydraulic Conductivity, Treated zone, k_{pl} (m/s)	1×10^{-4}

* Storage capacity is the amount of water that will be stored in the drain while it fills up, before water gets released in the surface.

2

3 **Table 2 Input parameters for DM2004 effective stress model after Vytiniotis (2012)**

DM2004 Model Parameters		
Category	Variable	Nevada Sand
	G_0	258
	ν	0.05
	M	1.25
	c	0.812
	λ_c	0.0022
	e_0	0.815
	ξ	1.54
	h_0	1.0
	c_h	0.988
	n^b	1.0
	A_0	0.25
	n^d	5.0
	z_{max}	3.0
	c_z	1.0
Yield Surface	m	0.01

* $D_r=80\%$; $e=0.5897$; $\gamma_t=2.07\text{Mg/m}^3$

** $D_r=40\%$; $e=0.7457$; $\gamma_t=1.98\text{Mg/m}^3$

4

1 **Table 3 Yolo loam elasto-plastic model properties after Vytiniotis (2012)**

Yolo Loam Parameters		
Category	Variable	Value
	G_{ref} (kPa)	13,000
	K_{ref} (kPa)	65,000
	Cohesion, c (kPa)	6
	γ_{peak}	0.1

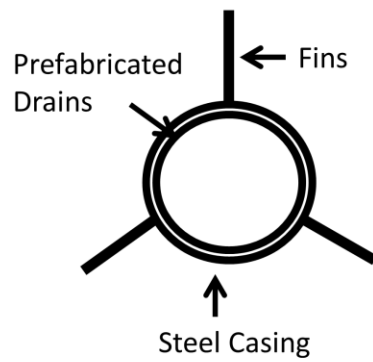
* $\gamma_t = 1.3 \text{ Mg/m}^3$

** Shear and bulk reference moduli are referenced at a mean effective stress of 100 kPa.

2 *** γ_{peak} is the shear strain mobilized at peak shear strength

3

a. Cross Section



b. Side View

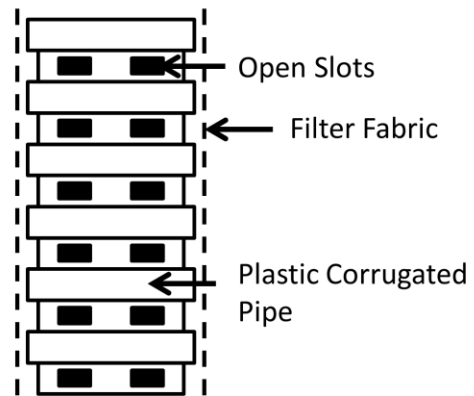


Fig. 1 PV drain schematic: a) Cross-section of casing and PV drain; and b) Side view

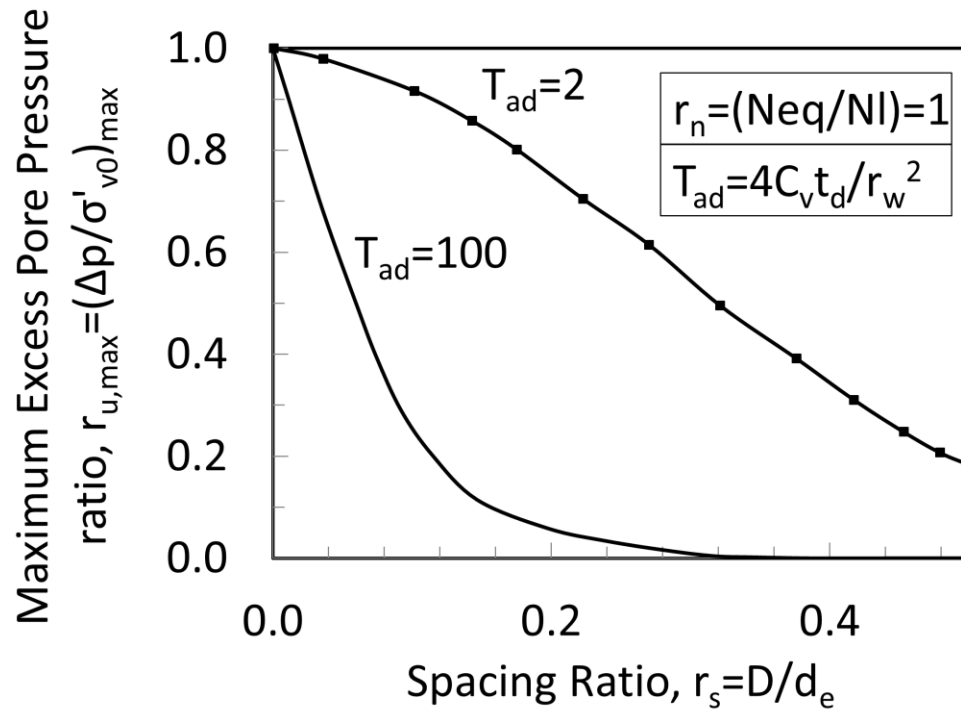


Fig. 2 Design for spacing of gravel drains to mitigate against liquefaction (after Seed & Booker, 1977).

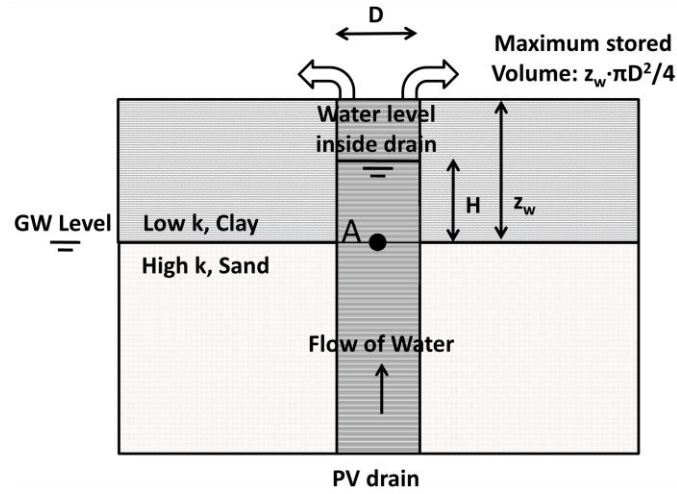


Fig. 3 Liquefaction mitigation through the use of earthquake drains illustrating drain storage capacity (Pestana et al., 1998)

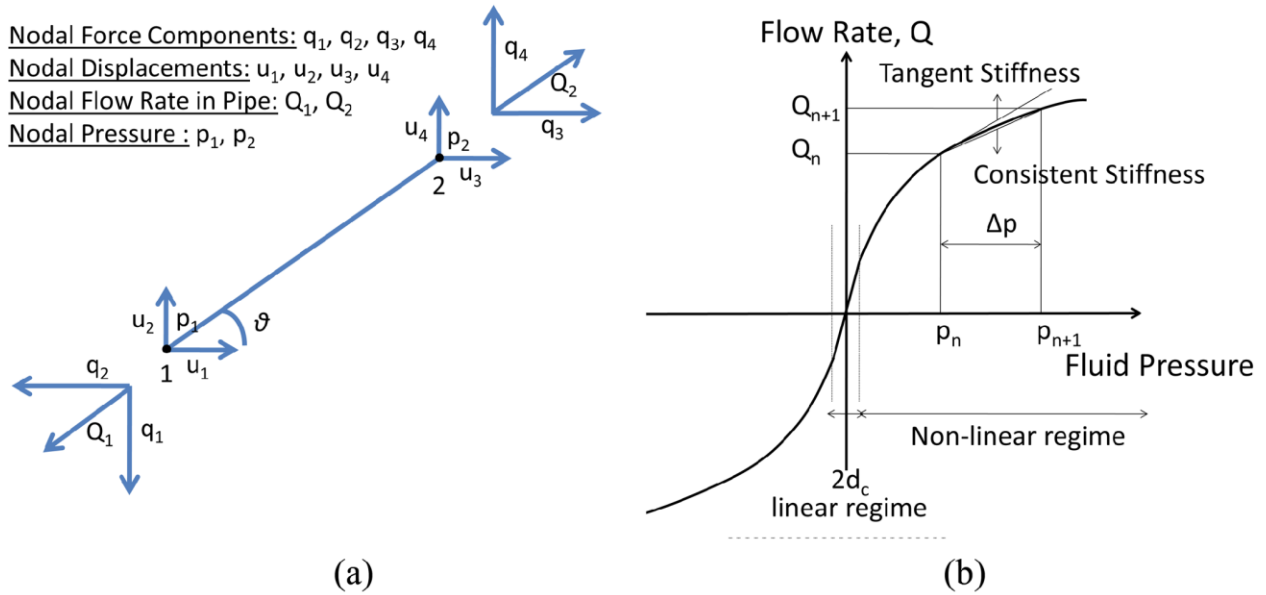


Fig. 4 Formulation of PV drain line element: a) notation; and b) flow regimes and discretization of flow

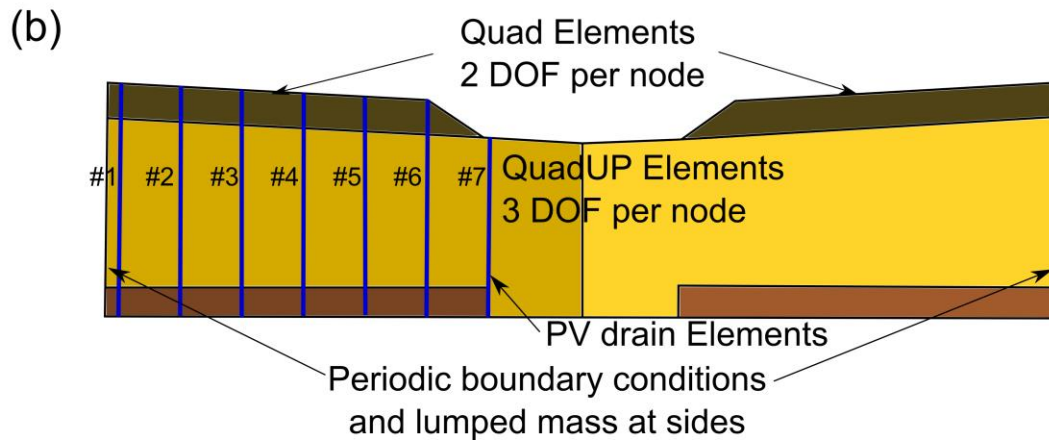
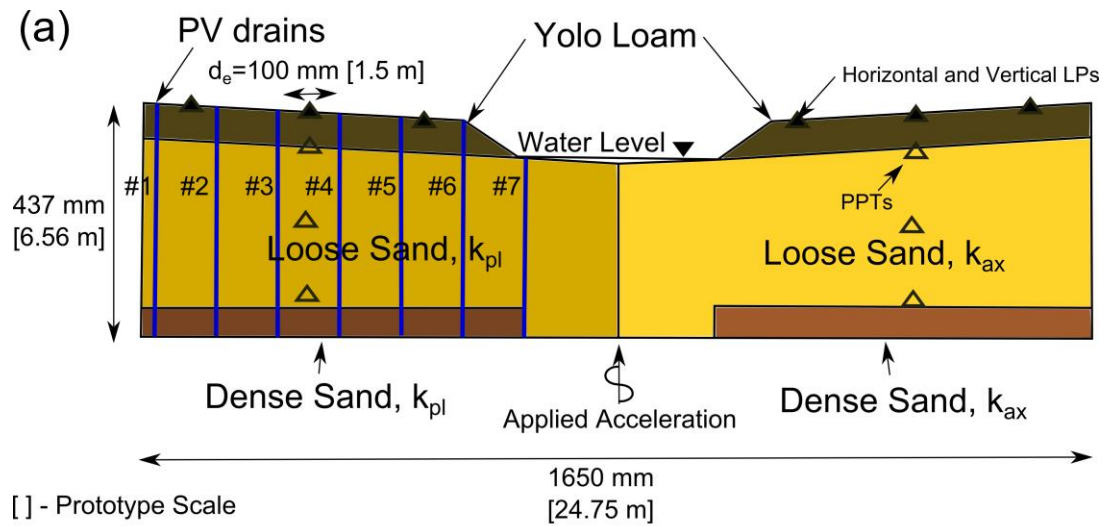


Fig. 5 Centrifuge model SSK01 to investigate effect of PV drain treatment on seismic site response: a) experimental configuration; and b) domains used in finite element model

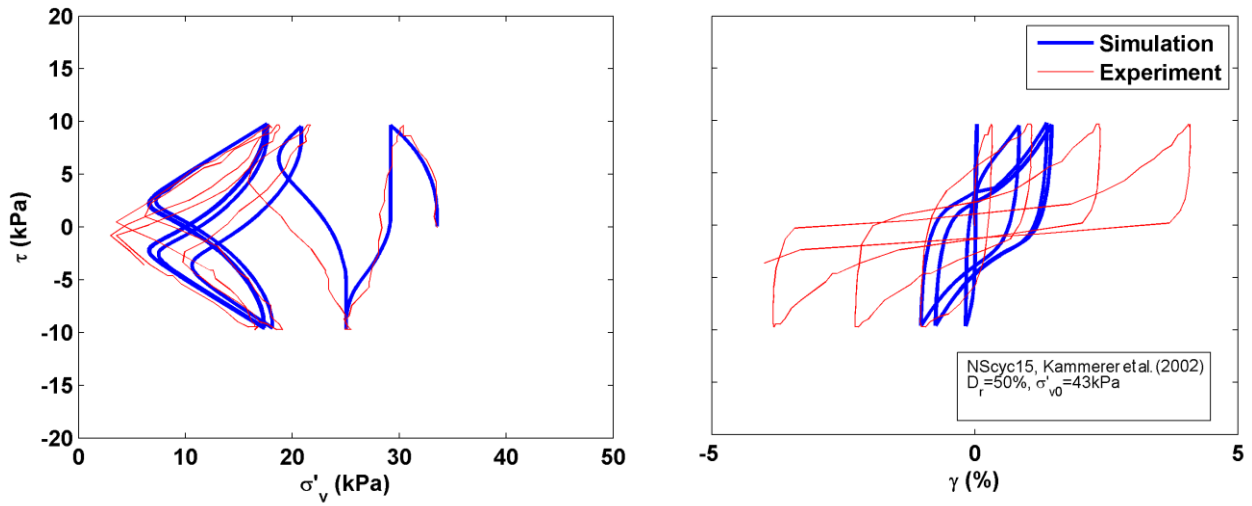


Fig. 6 Comparison of computed and measured shear response of Nevada sand ($D_r = 50\%$) in a cyclic direct simple shear test

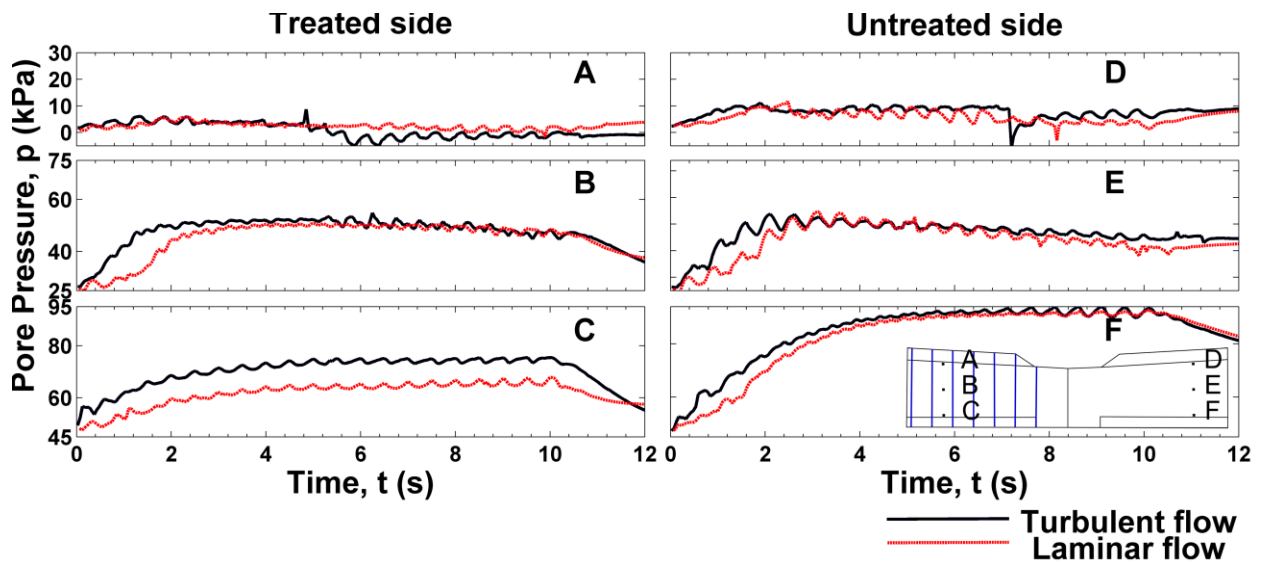


Fig. 7 Comparison of computed pore pressures in SSK01 model using fully turbulent and laminar PV drain elements during event SSK01_10

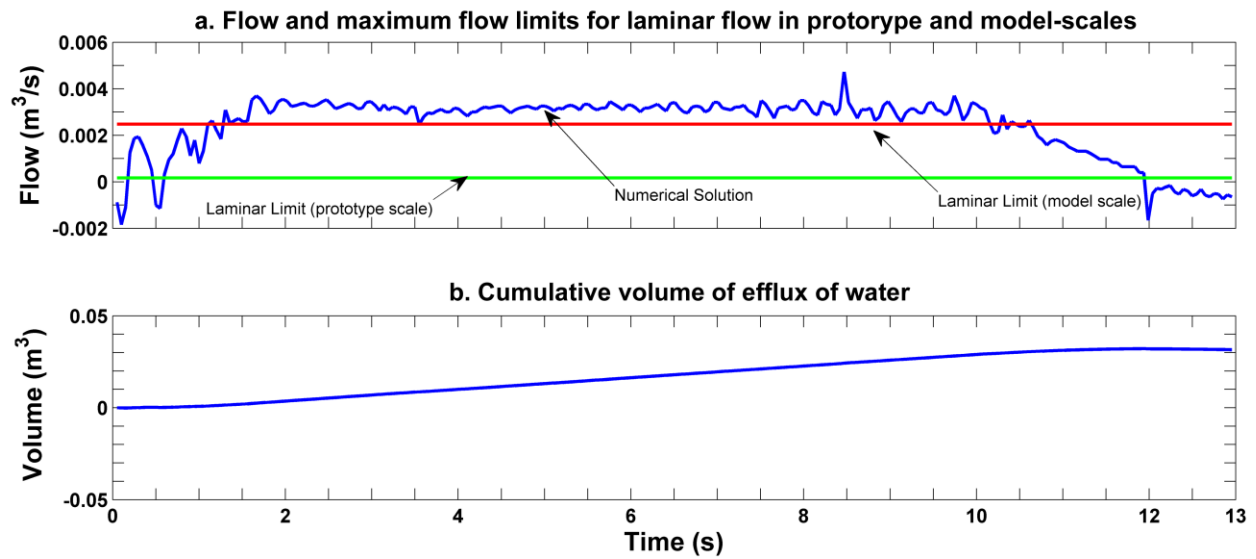


Fig. 8 Typical outflow results for row of drains #2: a) flow and maximum flow limits for laminar flow in prototype and model-scales; and b) cumulative volume of efflux water

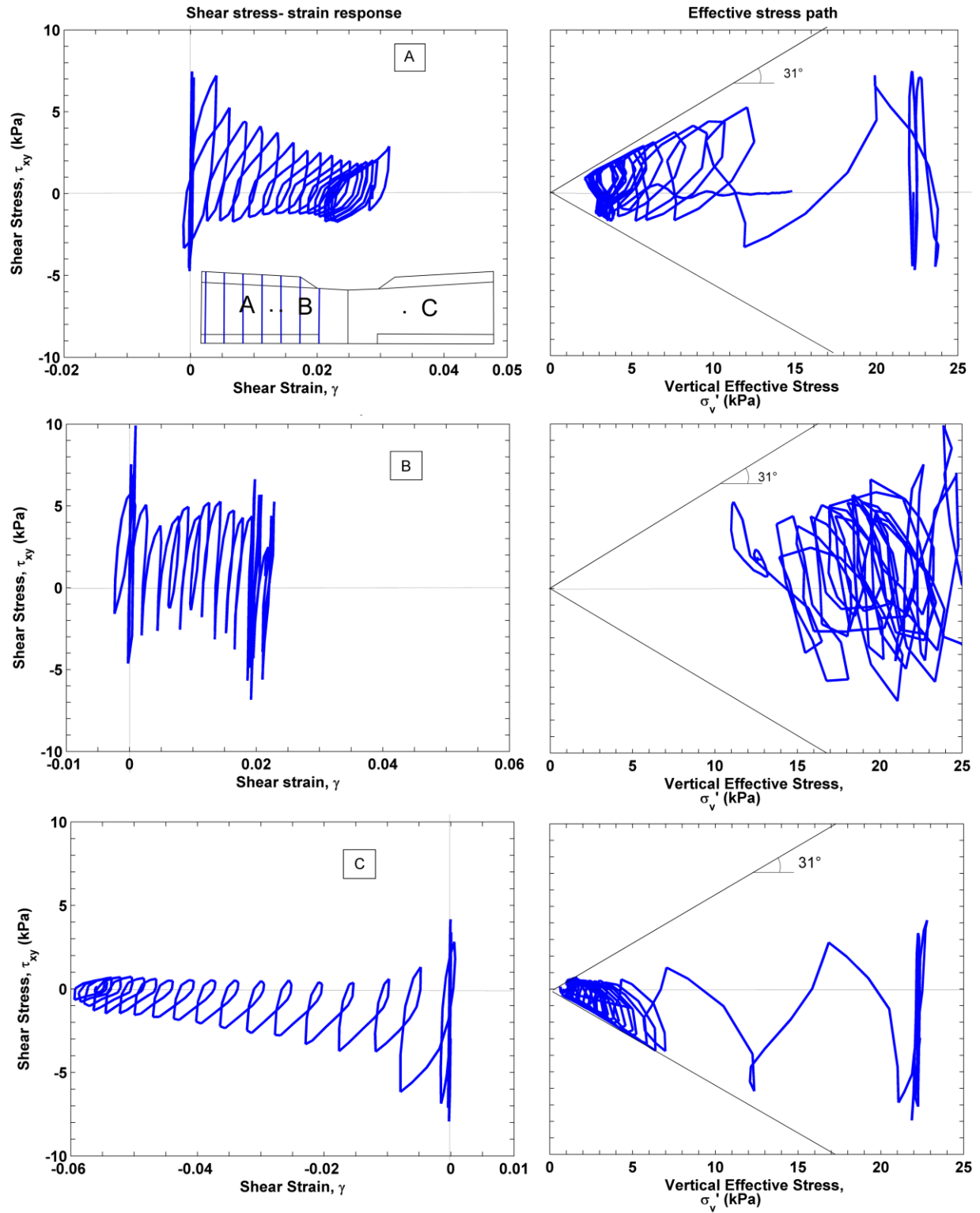


Fig. 9 Computed effective stress paths and shear stress-strain response at three location within the loose sand during event SSK01_10 (model assumes laminar flow in PV drains)

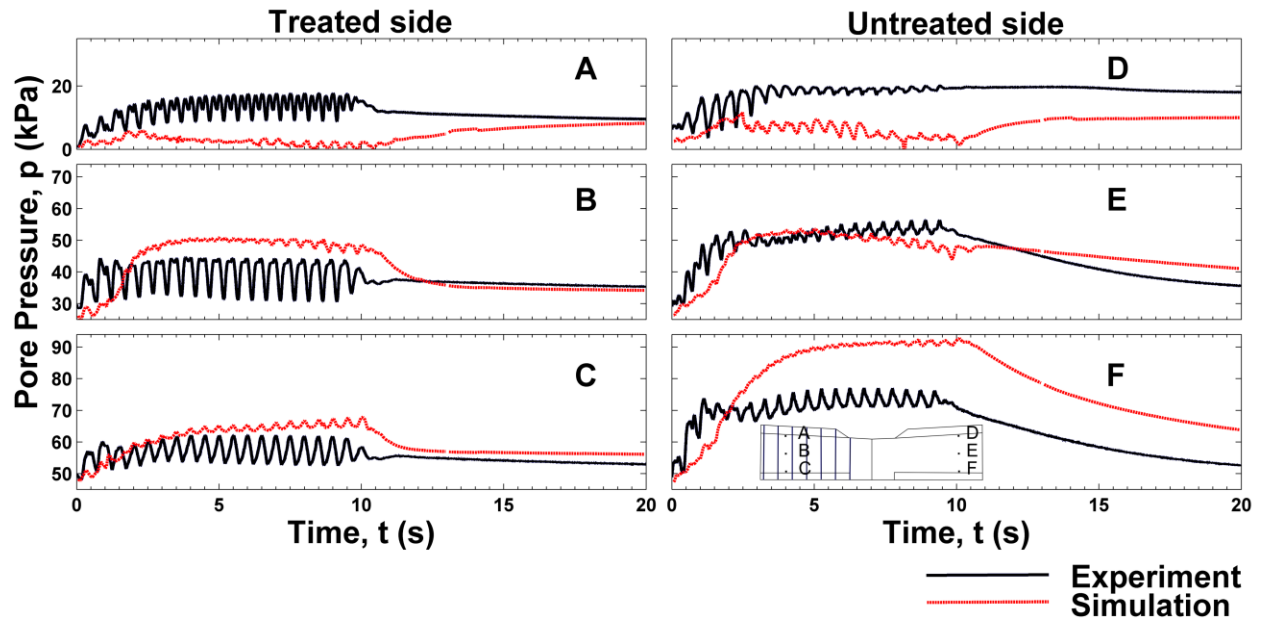


Fig. 10 Comparison of computed and measured pore pressures for centrifuge model during event SSK01_10 (model assumes laminar flow in PV drains)

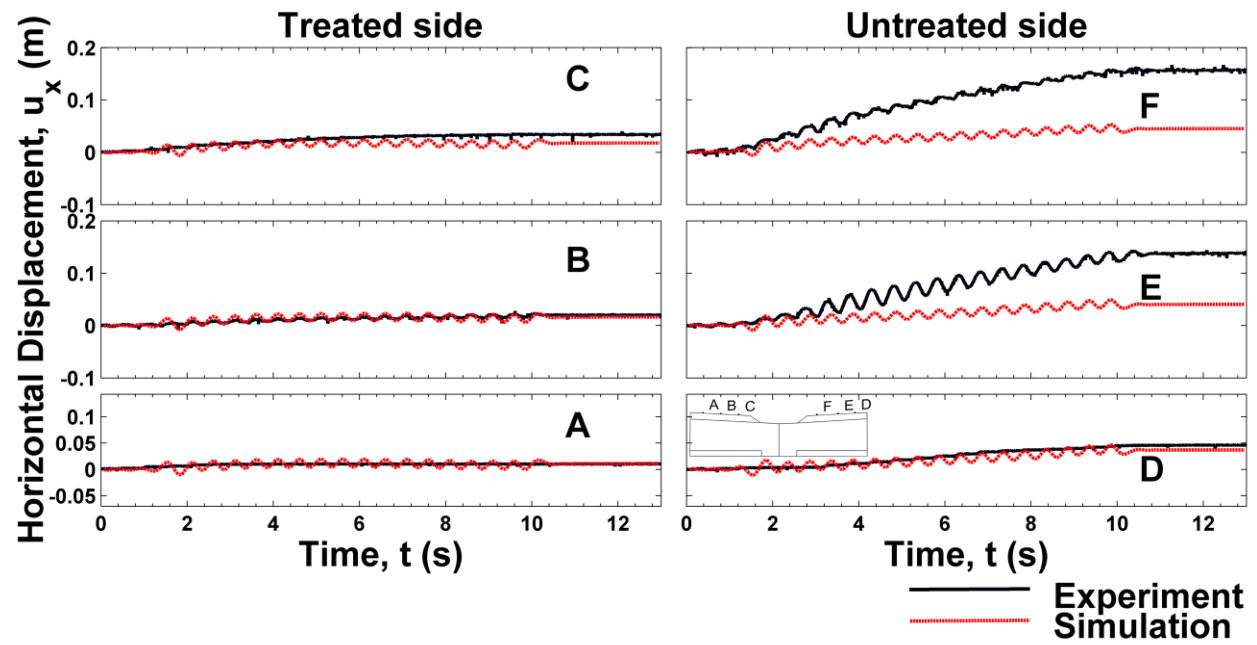


Fig. 11 Comparison of computed and measured horizontal surface displacements during event SSK01_10 (model assumes laminar flow in PV drains)

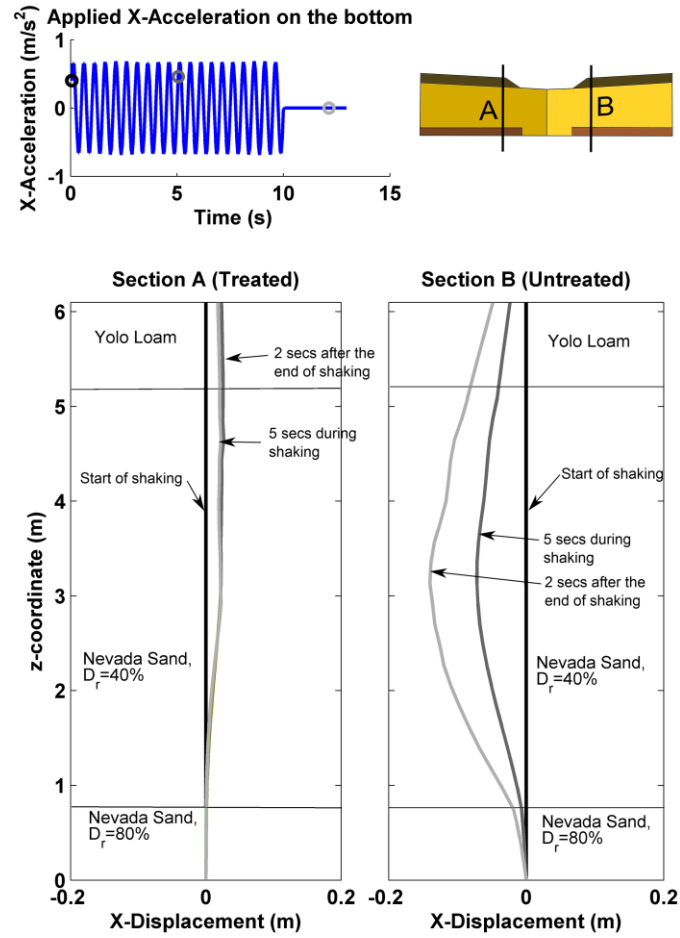


Fig. 12 Comparison of simulated horizontal displacement profiles at three selected times during shaking in event SSK01_10 (model assumes laminar flow in PV drains)

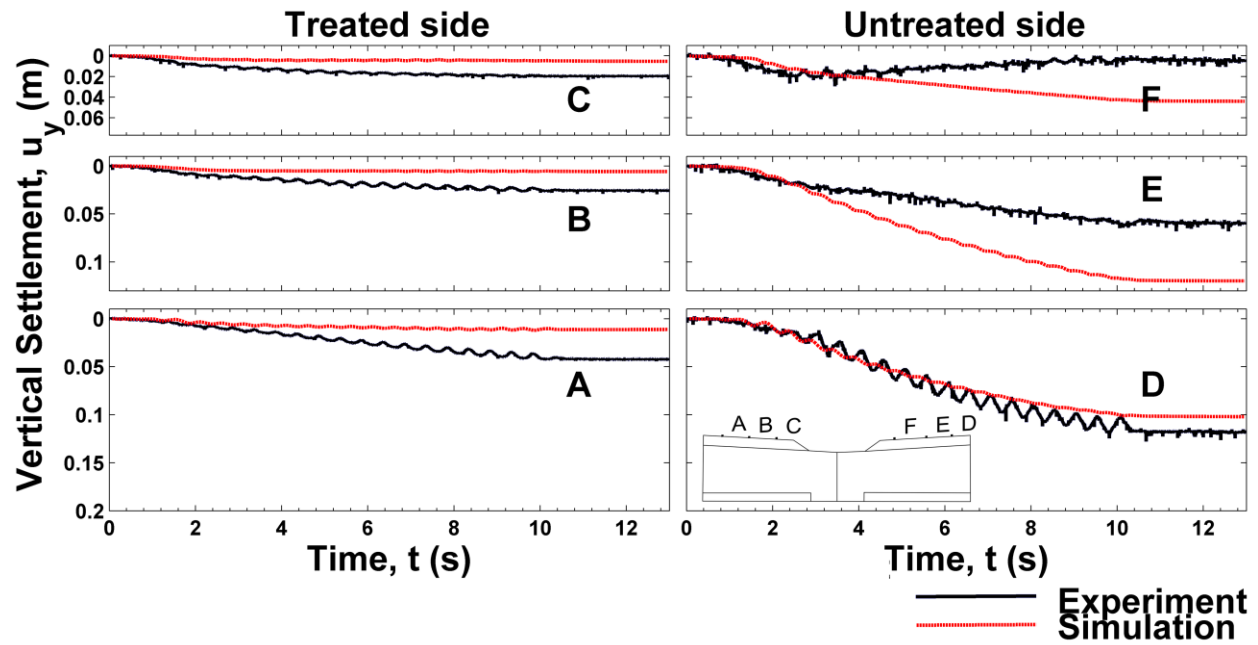


Fig. 13 Comparison of computed and measured vertical surface settlements for event SSK01_10 (model assumes laminar flow in PV drains)

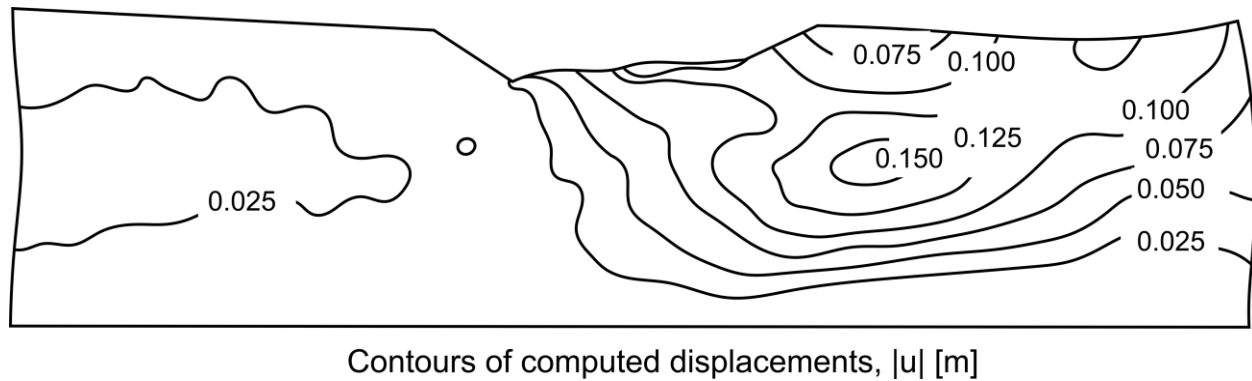


Fig. 14 Deformed shape (4x magnification) and displacement contours (in meters) after the end of the cyclic loading and dissipation